Article:
Haoting, L, Na, Z, Wang, Y et al. (4 more authors) (2021) Development of a face recognition system and its intelligent lighting compensation method for dark-field application. IEEE Transactions on Instrumentation and Measurement. ISSN 0018-9456

https://doi.org/10.1109/TIM.2021.3111076

Development of a face recognition system and its intelligent lighting compensation method for dark-field application

Haoting Liu, Na Zheng, Yuan Wang, Jiacheng Li, Zhiqiang Zhang, *Member, IEEE*, Yajie Li, and Jinhui Lan

***Abstract*—A face recognition system which uses 3D lighting estimation and optimal lighting compensation for dark-field application is proposed. To develop the proposed system, which can realize people identification in a near scene dark-field environment, a light-emitting diode (LED) overhead light, eight LED wall lights, a visible light binocular camera, and a control circuit are used. First, 68 facial landmarks are detected and their coordinates in both image as well as camera coordinate systems are computed. Second, a 3D morphable model (3DMM) is developed after considering facial shadows, and a transformation matrix between the 3DMM and camera coordinate systems is estimated. Third, to assess lighting uniformity, 30 evaluation points are selected from the face. Sequencing computations of LED radiation intensity, ray reflection luminance, camera response, and face lighting uniformity are then carried out. Ray occlusion is processed using a simplified 3D face model. Fourth, an optimal lighting compensation is realized: the overhead light is used for flood lighting, and the wall lights are employed as meticulous lighting. A genetic algorithm then is used to identify the optimal lighting of the wall lights. Finally, an Eigenface method is used for face recognition. The results show that our system and method can improve face recognition accuracy by >10% compared to traditional recognition methods.**

***Index Terms*—face recognition, distributed intelligent lighting, 3DMM, light compensation, dark-field environment**

I. Introduction

FACE recognition plays an important role for crime prevention and case investigation in the modern society [1]. Compared with other public management methods, face recognition is simple to use and can put criminals under tremendous mental pressure when they intend to commit a crime. Currently, face recognition always performs poorly when the lighting conditions are weak or complex. For example, if the surface illuminance of the face is ≤ 50.0 lx, a recognition algorithm may fail because many face details are covered by either shadows or glares. Fig. 1 shows examples of face image. In Fig. 1, (a) and (b) are influenced by shadows, whereas (c) is affected by non-uniform lighting; note that both shadow and glare can be observed. Unfortunately, criminals also take advantage of these limitations. A considerable amount of statistical data have shown juvenile delinquency in China always occurs at night in Karaoke bars or hotels [2]. Therefore, at these sites, if a robust face recognition system and method can be developed and used, the crime rate may be reduced.

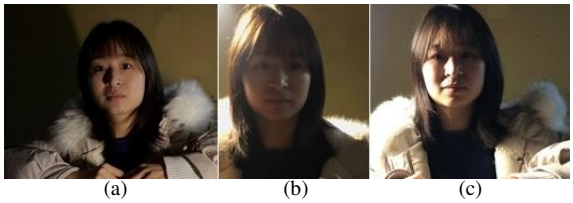

(a) (b) (c)

Fig. 1. Examples of degraded face image captured in the dark field.

Three types of techniques have been developed to solve the face recognition's limitations in dark environment in the past. The first technique used a proper sensor to capture high-quality images. Moreover, a near-infrared camera [3] and a multi-spectral camera [4] could be used. The second technique attempted to improve the computational effect of recognition algorithms. A data fusion-based method [5], a luminance processing-based technique [6], and a machine learning-based algorithm [7] were then developed. The third technique focused on designing an effective lighting source to compensate for poor lighting conditions. For example, in [8], an imaging definition feedback-based method was developed. Proper use of sensors can obtain images of better quality; however their costs are always high. Artificial intelligent algorithms, such as deep learning-based methods [9], can improve processing effect; however, their computational complexities inevitably add to the system's burden. Comparatively, a lighting design-based method is inexpensive and effective; and research in this regard is not as popular as the other two methods.

To improve the computational effect of imaging systems [10], certain adaptive lighting systems have been developed in

Manuscript received May 8, 2021; revised July 18, 2021; accepted ***. Date of publication ***; date of current version ***

This work was supported by the National Natural Science Foundation of China under Grant 61975011, the Fund of State Key Laboratory of Intense Pulsed Radiation Simulation and Effect under Grant SKLIPR2024, and the Fundamental Research Fund for the China Central Universities of USTB under Grant FRF-BD-19-002A.

H. Liu, N. Zheng, Y. Wang, J. Li, Y. Li, and J. Lan are with the Beijing Engineering Research Center of Industrial Spectrum Imaging, School of Automation and Electrical Engineering, University of Science and Technology Beijing, Beijing, 100083, China (e-mails: liuhaoting@ustb.edu.cn).

Z. Zhang and H. Liu are with the School of Electronic and Electrical Engineering, School of Mechanical Engineering, University of Leeds (*correspondence e-mails: eenzzh@leeds.ac.uk, liuhaoting@ustb.edu.cn).

Digital Object Identifier

the past. In [11], the authors employed near-infrared laser lighting to assist finger vein recognition. In [12], an adaptive lighting device was invented to realize the docking application of underwater vehicle. In [13], infrared light-emitting diodes (LEDs) were used to capture "red-eye" such that robust face recognition could be gotten. Currently, the researches of intelligent LED systems still face several challenges. The first problem is the lighting perception abilities of certain systems are still low. Both the environment lighting state and the surface light reflection character of a subject cannot be accurately estimated. To evaluate the lighting effect, many systems only use 2D images [14]. The second limitation lies in the poor control ability of LED lamps. There is no optimal model to obtain the control intensity of LEDs [15]. Third, narrow designs of lighting fields or negative influences of shadow and glare restrict these system's application. Because of these limitations, a new development of intelligent lighting systems is required.

In this study, a novel lighting system is proposed for face recognition in the dark field. It comprises one LED overhead light, eight LED wall lights, a visible light binocular camera, and a control circuit. First, face detection and facial landmark extraction [16] are performed. The histogram of oriented gradients (HOG), support vector machine (SVM), and ensemble of regression trees (ERT) are used. Second, a 3D face model and a transformation matrix between 3D faces and the camera coordinate systems are estimated. A 3D morphable model (3DMM) [17] with shadow analysis is then developed. Third, 3D face lighting effect estimation is performed. The LED radiation intensity [18], ray reflection luminance [19], camera response [20], and face lighting uniformity are then computed. Ray occlusion between the LED source and investigated point in the face is processed using a simplified 3D face model. Fourth, intelligent lighting control is performed. The overhead light is set to provide flood-lighting [21] and the wall lights provide optimal luminance compensation [22]. Finally, to identify the face, an Eigenface method [23] is used.

The primary contributions of this study are: 1) a novel 3D light field analysis-based intelligent lighting system which uses the visible light binocular camera and distributed LED units is proposed. 2) A complete mathematical model of optimal lighting estimation and compensation is developed, including ray radiation, ray reflection, ray occlusion, and ray distribution estimation. 3) Certain relationships about the lighting effect, face recognition accuracy, and vision interference issues are disclosed; factors, such as the overhead light output intensity, the spatial position relationship between the wall lights and face, and the lighting uniformity, etc., are investigated.

In the following sections, first, the problem definition and system design will be presented. Second, the intelligent lighting control method will be shown. Third, the experimental results and discussions will be provided.

II. Problem Formulation and Proposed System

A. Problem Formulation

Fig. 2 shows the sketch maps of the face recognition application in the dark field and the system design method. In Fig. 2-(a), an imaginary picture of the proposed application is presented. This system can then be used to identify people who come to the information desk in a Karaoke bar or a hotel. For example, a waitress stands behind a table with her back to a wall and a visitor inquires something from her. In certain cases, the lighting conditions in a Karaoke bar or hotel may be poor to create a relaxing atmosphere. For example, the environment illuminance is only 30.0 - 60.0 lx. In Fig. 2-(b), a system constitution method is shown. A LED overhead light is used to provide flood-lighting; eight LED point lights in the wall are considered to configure a proper compensation source for face recognition. A visible light binocular camera is used to capture face images and estimate the 3D coordinate of typical facial landmarks. All the light sources and the camera system are connected by a wireless communication device. If the environment lighting can be well compensated, an ideal face image can be created.

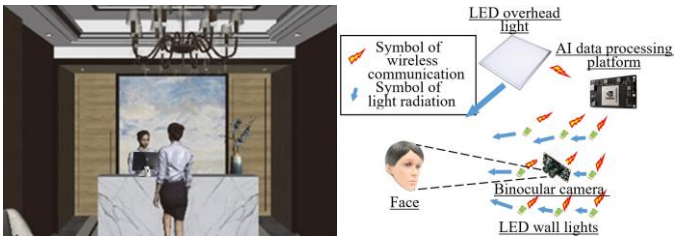

Fig. 2. Imaginary picture of face recognition application in the dark field and sketch map of our proposed system.

B. Distributed Lighting and Face Recognition System

Fig. 3 shows a sketch map of the proposed distributed lighting and face recognition system. In Fig. 3, (a) and (c) are the side view and the top view of this system, respectively; (b) is the design method of wall lights; and (d) is the top view of our application with a roof. The parameters D_i (i = 0, 1, …, 11) define the distance or length variables in the application. As shown in Fig. 2-(a), because the waitress requires to assess information on a computer, she has to stand in front of a display; moreover, a visitor has to stand in the left or the right side of that display such that he or she can directly face the waitress. In this situation, the visitor's face can be exposed to the wall lights. Without loss of generality, the output tuning methods of the overhead light and wall lights have certain fixed degrees. For example, they have 3 degrees and 6 degrees, respectively. The control method of the wall lights is more flexible. A plane and symmetrical design mode is considered for the distributed wall lights. The binocular vision system has one camera positioned in the geometric center of the wall light array.

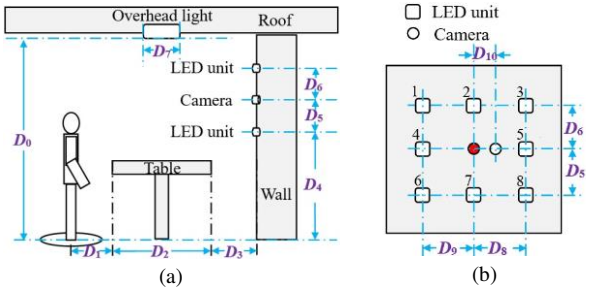

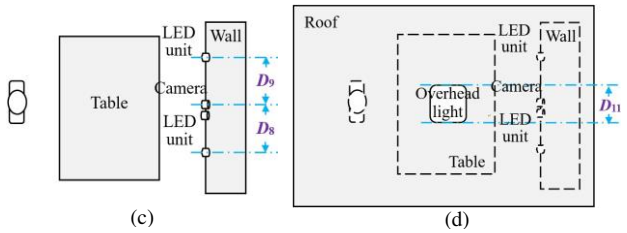

(c) (d)

Fig. 3. Sketch map of the distributed lighting and face recognition system.

III. Proposed Face Recognition Method with Intelligent Lighting Compensation

A. The Overall Computational Framework

Fig. 4 presents the overall computational framework of the proposed system and method. Our computations include four steps. First, the fast face detection and facial landmark extraction are performed. This step can yield the initial face region and extract 68 2D and 3D facial landmarks in an image and the camera coordinate systems, respectively. Second, a 3D face model and a coordinate system transformation matrix are constructed and calculated. This step can estimate a complete 3D face model and compute the transformation matrix between the 3D face model and the camera coordinate systems. Third, face lighting effect evaluation is conducted. This step can simulate the face lighting effect of 30 typical facial landmarks and estimate a lighting uniformity index using any simulated LED intensity input. Fourth, intelligent lighting compensation and face recognition are implemented. This step can then tune flood-lighting and meticulous lighting to achieve robust face recognition in the dark field. In Fig. 4, contents within the red dash rectangle are our proposed steps, which can achieve intelligent lighting compensation, whereas other contents belong to the traditional processing steps of face recognition.

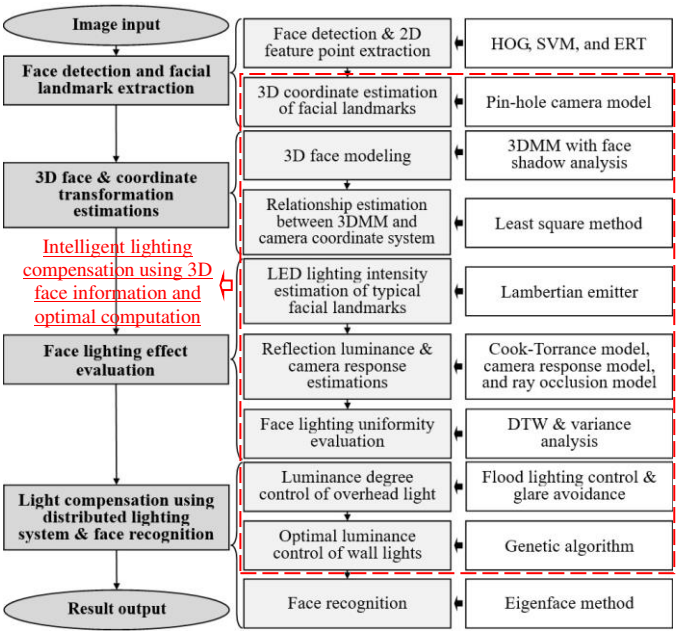

Fig. 4. Proposed computational flow chart.

B. Face Detection and Facial Landmark Extraction

When implementing face detection, three methods are commonly used: Harr feature and AdaBoost, HOG features and SVM, and deep learning-based methods. Among these methods, the SVM classifier can achieve a high classification accuracy only with a limited amount of training data, whereas other methods need high image quality or large training data input; thus, SVM is used in our system. When performing 2D facial landmark extraction, a facial landmark template is first defined; then, an ERT is used to fit the contour of the face in an image via iterative computations. Finally, 68 facial 2D points are identified. A visible light binocular camera is used to estimate 3D facial landmarks. The Zhang et al.'s method [24] is used to calibrate the binocular vision system first. Then we incorporate the world coordinate system into one of the camera coordinate systems, and then, 3D facial landmarks can be calculated from 2D landmarks using (1). Fig. 5 shows the definition of 68 facial landmarks and their 2D and 3D samples in an actual face image.

$$s\begin{bmatrix} x \\ y \\ 1 \end{bmatrix} = \begin{bmatrix} f_x & 0 & u_0 \\ 0 & f_y & v_0 \\ 0 & 0 & 1 \end{bmatrix} [R \mid T] \begin{bmatrix} U \\ V \\ W \\ 1 \end{bmatrix} \quad (1)$$

where (x, y) is a coordinate in the image coordinate system; (U, V, W) is a coordinate in the world coordinate system; s is a scale factor; f_x, f_y are the camera focal lengths; u_0 and v_0 are the principal point coordinates in the x and y directions. Note that R is a rotation matrix and its sub-variables can be defined by r_{ij} $(i, j = 0, 1, 2)$, whereas $T = [t_0, t_1, t_2]$ is a translation matrix.

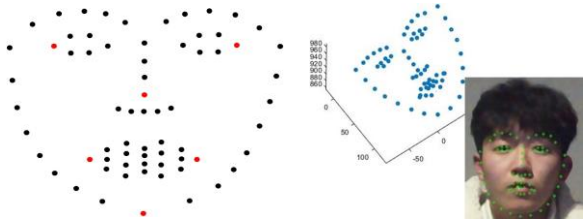

(a) (b)

Fig. 5. Definition of facial landmarks and their 2D and 3D results in an actual face image.

C. 3D Face Model and Coordinate Transformation Estimation

3DMM is used for 3D face modeling. It is a classic model that can represent the face by a 3D dense point cloud. Generally, a 3DMM can be defined by a mean face and a linear weighted sum of the shape and expression factors. In this study, the Basel face model (BFM) [25] is used as the mean face; then, the estimation of the 3DMM transforms into an iterative computation of the shape and expression factors. This step can realize coordinate calculations from 68 2D facial landmarks to the corresponding 3D coordinate points in the 3DMM coordinate system. Because the binocular camera is used in our system, it is necessary to build a transformation relationship between the 3DMM coordinate system and the camera coordinate system such that we can transfer any spatial points from one coordinate system to the other. Equation (2) presents the computational method of the transformation matrix; the least squares method can be used to obtain the rotation and translation matrices.

$$M_{Cam} = R_{Cam\_3DMM} M_{3DMM} + T_{Cam\_3DMM} \quad (2)$$

where M_{3DMM} is the 3D coordinate in the 3DMM coordinate system; M_{Cam} is the 3D coordinate in the camera coordinate system; R_{Cam_3DMM} and T_{Cam_3DMM} are the rotation and transformation matrices, respectively.

The shadow will affect the estimation of 3DMM severely in dark field: if an image contrast is low, the estimations of 68 facial landmarks will be inaccurate. To overcome limitation, shadow analysis-based enhancement is developed. Both a multiple-scale Retinex (MSR) [26] and SVM are considered. First, potential shadow features around the eyes, nose, and mouth are computed. Gray means in the typical face blocks are examined. Fig. 6 shows the sketch map and the image sampling method of MSR computational blocks. Their order numbers of MSR blocks are also demonstrated. Second, SVM is trained to predict the control parameters of MSR using the gray features above. Equations (3) and (4) show the MSR model. In this study, l_1, l_2, l_3, ε_1, and ε_2 are set with certain fixed experiential values, whereas ε_3 is regarded as a control parameter. The inputs of SVM are the gray means of shadow blocks, and its output is ε_3. Finally, an adaptive MSR after considering face shadows is developed.

$$R(i,j) = \sum_{k=1}^{3} l_k \left\{ \lg I(i,j) - \lg\left[G_k(i,j) * I(i,j) \right] \right\} \quad (3)$$

$$G_k(i,j) = \frac{1}{2\pi\varepsilon_k^2} \exp\left(-\frac{i^2 + j^2}{2\varepsilon_k^2} \right) \quad (4)$$

where l_k and ε_k are the weight and scale factors with k = 1, 2, 3, $l_1 + l_2 + l_3 = 1$; $I(i, j)$ is the image; $G_k(i, j)$ is a low-pass Gaussian filter; and the symbol '*' is the convolution operation.

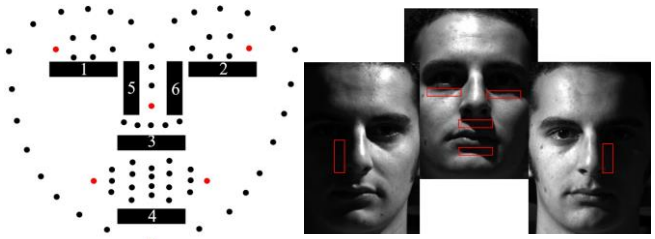

(a) (b)

Fig. 6. Proposed shadow analysis method and some image examples [27].

D. Face Lighting Effect Evaluation

The face lighting effect evaluation can realize complete computations from LED ray radiation to camera ray response.

● LED lighting effect computation

In this study, the LED bead is considered as a Lambertian emitter [28]. Without loss of generality, it is supposed that the LED bead is a symmetrical source; ideally, it is a point source for the wall light application. Because the size of each LED bead is ≤ 1.0 cm, whereas the observation distance is always ≥ 100.0 cm, it can be considered as a point light source. Fig. 3-(b) shows the arrangement of wall light LED beads, and their order numbers are illustrated; it is supposed all beads have the same optic performance. A camera coordinate system is then defined in a camera that is marked by a red solid circle: its z-axis is perpendicular to the wall light panel, and its x- and y-axes are parallel to the rectangle edges of that panel. In the following computations, all other coordinate systems will be transformed into this camera coordinate system. Finally, the radiance intensity E_{Wall} of all LED beads can be estimated using the arithmetic sum of a single LED output since the wall lights lie in the same working plane. Equation (5) shows the radiation intensity definition of wall lights. It is defined in the camera coordinate system.

$$\begin{aligned}
E_{Wall} = {} & z_W^{m_W} I_{WL_0} A_{WL_0} \left[\left(x_W - \frac{d_W}{2} \right)^2 + y_W^2 + z_W^2 \right]^{-\frac{m_W+2}{2}} + \\
& z_W^{m_W} I_{WL_1} A_{WL_1} \left[\left(x_W - \frac{d_W}{2} \right)^2 + \left(y_W - \frac{d_W}{2} \right)^2 + z_W^2 \right]^{-\frac{m_W+2}{2}} + \\
& z_W^{m_W} I_{WL_2} A_{WL_2} \left[x_W^2 + \left(y_W - \frac{d_W}{2} \right)^2 + z_W^2 \right]^{-\frac{m_W+2}{2}} + \\
& z_W^{m_W} I_{WL_3} A_{WL_3} \left[\left(x_W + \frac{d_W}{2} \right)^2 + \left(y_W - \frac{d_W}{2} \right)^2 + z_W^2 \right]^{-\frac{m_W+2}{2}} + \\
& z_W^{m_W} I_{WL_4} A_{WL_4} \left[\left(x_W + \frac{d_W}{2} \right)^2 + y_W^2 + z_W^2 \right]^{-\frac{m_W+2}{2}} + \\
& z_W^{m_W} I_{WL_5} A_{WL_5} \left[\left(x_W + \frac{d_W}{2} \right)^2 + \left(y_W + \frac{d_W}{2} \right)^2 + z_W^2 \right]^{-\frac{m_W+2}{2}} + \\
& z_W^{m_W} I_{WL_6} A_{WL_6} \left[x_W^2 + \left(y_W + \frac{d_W}{2} \right)^2 + z_W^2 \right]^{-\frac{m_W+2}{2}} + \\
& z_W^{m_W} I_{WL_7} A_{WL_7} \left[\left(x_W - \frac{d_W}{2} \right)^2 + \left(y_W + \frac{d_W}{2} \right)^2 + z_W^2 \right]^{-\frac{m_W+2}{2}}
\end{aligned} \quad (5)$$

where m_W represents a parameter that can reflect the relationship between the view angle and radiance attenuation, and m_W= 32.0 in this study; (x_W, y_W, z_W) is a spatial coordinate of observation point in the wall light coordinate system, with z_W > 0; I_{WL_i} and A_{WL_i} (i = 0, 1, …, 7) are the intensity output and the emitting area factors of the i^{th} LED bead, with $A_{WL\_0} = A_{WL\_1} = \ldots = A_{WL\_7} = 1.0$; $d_W = D_5 = D_6 = D_8 = D_9$ (see Fig. 3 (b)).

The overhead light is used to provide flood-lighting and avoid glare in our application. Fig. 3-(a) shows that the overhead light is installed in the front top side of a visitor which can guarantee a comparable good face lighting effect. The overhead light is developed using a rectangle array with M×N LED beads; the intensity output of all LED beads should be equally controlled in the same lighting effect degree; its output intensity only has 3 degrees in our application for simplicity. Similar to the coordinate system definition of the wall light plane, the original point of the overhead light coordinate system

is defined in its geometric center, the *x*- and the *y*-axes are parallel to the edges of rectangle array, and the *z*-axis is perpendicular to the *x*-*y* plane. Then, the radiance intensity of the overhead light $E_{Overhead}$ is defined by (6). To estimate the lighting effect, a coordinate transform in (7) is performed; and then the intensity sum E_s in (8) can be calculated to represent a complete LED radiance intensity of both the wall and the overhead lights.

$$E_{Overhead} = z_0^{m_0} I_{OL} A_{OL} \times \sum_{i=1}^{N}\sum_{j=1}^{M} \left\{ \begin{bmatrix} x_0 - \left(N+1-2i\right)\times\dfrac{d_0}{2} \end{bmatrix}^2 + \begin{bmatrix} y_0 - \left(M+1-2j\right)\times\dfrac{d_0}{2} \end{bmatrix}^2 + z_0^2 \right\}^{-\frac{m_0+2}{2}} \quad (6)$$

$$\begin{bmatrix} x_O \\ y_O \\ z_O \end{bmatrix} = \begin{bmatrix} 1 & 0 & 0 \\ 0 & 0 & 1 \\ 0 & -1 & 0 \end{bmatrix} \begin{bmatrix} x_W \\ y_W \\ z_W \end{bmatrix} + \begin{bmatrix} X_S \\ Y_S \\ Z_S \end{bmatrix} \quad (7)$$

$$E_s = E_{Wall} + E'_{Overhead} \quad (8)$$

where (x_O, y_O, z_O) is the point coordinate in the overhead light coordinate system; m_O is a parameter, and m_O = 35.0; I_{OL} and A_{OL} are the intensity and emitting area factors of the overhead LED, and A_{OL} = 1.1; *M* and *N* are the sizes of the overhead LED array, and *M* = *N* = 3; (X_S, Y_S, Z_S) is a translation vector between a point in the wall light coordinate system and a point in the overhead light system; Note that $E'_{Overhead}$ is a coordinate transformation result of $E_{Overhead}$ after computing (7).

● Reflection luminance and camera response calculations

Reflection luminance is a function of the incident angle, reflection angle, and light wavelength. To improve its estimation accuracy, the bidirectional reflectance distribution function is used; in particular, the Cook-Torrance model [29] is considered. Fig. 7 shows the geometric sketch map of the Cook-Torrance model. According to the Cook-Torrance model, only the microplanes facing to the observation direction or the line of reflection direction contribute to the surface reflection intensity; thus, it can simplify the simulation procedure and improve the computation speed effectively. The definition of reflection luminance is shown in (9), and its specular reflection functions are illustrated in (10) - (13). The surface material character of skin can be represented by the refractive index. Moreover, a camera response model is constructed in this study. Equation (14) shows its computational method. Finally, pixel response intensities of any observation point in the 3DMM can be estimated.

$$L_i = \sum_{j=1}^{K} R_{C\_T\_ij} E_{s\_j} \cos\delta_{ij} \quad (9)$$

$$R_{C\_T\_ij} = \frac{F_{ij}}{\pi} \frac{D_{ij} G_{ij}}{\left(\boldsymbol{N}_i \cdot \boldsymbol{L}_{ij}\right)\left(\boldsymbol{N}_i \cdot \boldsymbol{V}_i\right)} \quad (10)$$

$$F_{ij} = \left(\frac{n_1 - n_2}{n_1 + n_2}\right)^2 + \left[1 - \left(\frac{n_1 - n_2}{n_1 + n_2}\right)^2\right]\left[1 - \left(\boldsymbol{N}_i \cdot \boldsymbol{L}_{ij}\right)\right]^5 \quad (11)$$

$$D_{ij} = \frac{1}{\pi r^2 \left(\boldsymbol{N}_i \cdot \boldsymbol{H}_{ij}\right)^4} \exp\left(\frac{\left(\boldsymbol{N}_i \cdot \boldsymbol{H}_{ij}\right)^2 - 1}{r^2 \left(\boldsymbol{N}_i \cdot \boldsymbol{H}_{ij}\right)^2}\right) \quad (12)$$

$$G_{ij} = \min\left(1, \frac{2\left(\boldsymbol{N}_i \cdot \boldsymbol{H}_{ij}\right)\left(\boldsymbol{N}_i \cdot \boldsymbol{V}_i\right)}{\boldsymbol{V}_i \cdot \boldsymbol{H}_{ij}}, \frac{2\left(\boldsymbol{N}_i \cdot \boldsymbol{H}_{ij}\right)\left(\boldsymbol{N}_i \cdot \boldsymbol{L}_j\right)}{\boldsymbol{V}_i \cdot \boldsymbol{H}_{ij}}\right) \quad (13)$$

$$I_i = L_i \frac{\pi}{4}\left(\frac{d}{h}\right)^2 \cos^4\varphi_i \quad (14)$$

where L_i represents the reflected radiance of the *i*th observation point; *K* is the light source number; $R_{C\_T\_ij}$ is the Cook-Torrance value of the *i*th observation point under the influence of the *j*th light source; δ_{ij} is an angle between the facet normal of the *i*th observation point and the connection line of the *i*th observation point and the *j*th light source; F_{ij} is the Fresnel coefficient; D_{ij} is the facet slope distribution function; G_{ij} is the geometrical attenuation factor; $\boldsymbol{N}_i$ is a unit vector denoting the facet normal of the *i*th observation point; $\boldsymbol{L}_{ij}$ is a unit vector that indicates the illumination direction between the *i*th observed point and *j*th light source; $\boldsymbol{V}_i$ is a unit vector representing the camera viewing direction of *i*th observation point; n_1 and n_2 are refractive indexes, with n_1 = 0.5 and n_2 = 1.00029; *r* is a surface roughness index, with *r* = 3.2; $\boldsymbol{H}_{ij}$ is a unit vector which is the bisector of $\boldsymbol{L}_{ij}$ and $\boldsymbol{V}_i$; min (A, B) can obtain the minimum value between A and B; I_i is the camera response of *i*th observation point; *h* is the focal length of the camera, and *h* = 0.31 mm; *d* is the camera aperture diameter, and *d* = 2.0 mm; φ_i is the off-axis angle between the camera optical axis and the connection line of the camera optic center and the *i*th observation point.

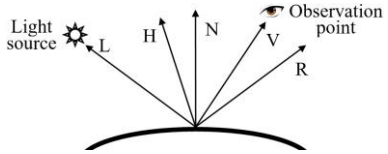

Fig. 7. Geometric sketch map of the Cook-Torrance model.

Ray occlusion should be identified from our application. In many cases, ray occlusion may occur when the LED ray is blocked by the cheek or the nose. If a visitor does not directly face the central camera, or slightly turns his or her face to another side from the wall lights, ray occlusion may be observed. In this study, we simplify the face using an ellipsoid and a triangular pyramid to achieve a fast computation. Fig. 8 shows the sketch map of this method. The triangular pyramid can be considered as three planes in space. The connection plane between the ellipsoid and the triangular pyramid will not be used in ray occlusion estimation. When performing ray occlusion evaluation, we only require to compute the intersection point between the ray and ellipsoid or any other three planes; if ray occlusion occurs, reflection luminance should be 0. Equations (15) and (16) are the computational methods of the ellipsoid and plane. Sixty-eight facial landmarks can be used to estimate their parameters because they can provide the corresponding spatial point coordinates close to the face edge or the nose.

$$f\left(x, y, z\right) = a_0 x^2 + a_1 y^2 + a_2 z^2 + a_3 xy + a_4 xz +$$

$$a_5yz + a_6x + a_7y + a_8z + a_9 \tag{15}$$

$$\begin{vmatrix} x - x_1 & y - y_1 & z - z_1 \\ x_2 - x_1 & y_2 - y_1 & z_2 - z_1 \\ x_3 - x_1 & y_3 - y_1 & z_3 - z_1 \end{vmatrix} = 0 \tag{16}$$

where (x, y, z) is a spatial coordinate; symbols a_i ($i = 0, 1, \ldots, 9$) are the parameters of the ellipsoid; (x_1, y_1, z_1), (x_2, y_2, z_2), and (x_3, y_3, z_3) are the known spatial point coordinates in the face.

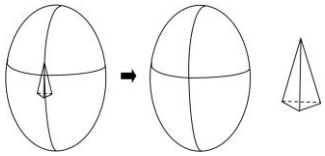

Fig. 8. Sketch map of the simplified face model.

● Face lighting uniformity estimation

A series of lighting uniformity observation points (LUOPs) are selected from the face to assess the lighting effect of LEDs. Fig. 9 shows the sketch map of LUOPs and their image examples: 30 LUOPs are selected, and they are captured from the forehead, eyes, nose, cheek, mouth, and chin. The dynamic time warping (DTW) [30] method is used to evaluate the lighting uniformity: first, a series of face images captured from the normal lighting effect are accumulated. For example, they are recorded when the environment illuminance is either ≥ 250.0 lx or 300.0 lx. Second, 30 LUOPs are selected from the above images, the average gray intensity of each observation point is computed. Third, we arrange these averages above in a one-dimensional coordinate system as per their order numbers, and then a standard response series can be obtained. Finally, the DTW is used to evaluate the similarity between the standard series and the new series captured from the arbitrary face. Moreover, the variance is computed by (17) and (18), as shown in Table 1, for lighting effect estimation. In (17), the variables VAR_i ($i = 1, 2, \ldots, 6$) represent the lighting uniformity, whereas $1/VAR_7$ indicates the intensity contrast.

$$M_F = w_1 M_{DTW} + w_2 M_{VAR} = w_1 M_{DTW} + w_2 \frac{\sum_{i=1}^{6} VAR_i}{VAR_7} \tag{17}$$

$$VAR_7 = VAR\left(MEAN_1, MEAN_2, MEAN_3, MEAN_4\right) \tag{18}$$

where w_1 and w_2 are the weights, with $w_1 = 0.1$ and $w_2 = 0.9$; M_{DTW} and M_{VAR} are the estimation results of DTW and variance, respectively; VAR_i ($i = 1, 2, \ldots, 6$), VAR, and $MEAN_j$ ($j = 1, 2, 3, 4$) are functions that can compute the variance and mean of image data, and their definitions are shown in Table 1.

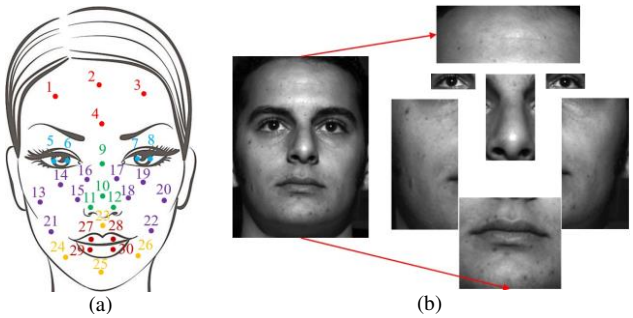

(a) (b)

Fig. 9. Sketch map of LUOPs and some image samples.

TABLE I
COMPUTATION METHOD OF FACE LIGHTING UNIFORMITY ESTIMATION

Function name	The facial landmarks that participate the variance or mean computation in equations (17) and (18)
VAR_1	{1, 2, 3, 4}
VAR_2	{5, 6, 7, 8}
VAR_3	{9, 10, 11, 12}
VAR_4	{13, 14, 15, 16, 17, 18, 19, 20, 21, 22}
VAR_5	{23, 24, 25, 26}
VAR_6	{27, 28, 29, 30}
$MEAN_1$	{1, 2, 3, 4, 13, 14, 15, 16, 17, 18, 19, 20, 21, 22, 23, 24, 25, 26}
$MEAN_2$	{5, 6, 7, 8}
$MEAN_3$	{9, 10, 11, 12}
$MEAN_4$	{27, 28, 29, 30}

E. The Intelligent Light Compensation and Face Recognition

Different control strategies are used for our lights. Because the illuminance output of overhead light should obey the management requirement of entertainment places in China, only three fixed lighting modes are used. For the wall lights, an optimal control method is designed by (19). The genetic algorithm [31] is used to estimate the optimal solutions of eight LED wall lights. The genetic algorithm is considered because it can accomplish a non-linear optimal estimation and achieve a stable processing effect. In this study, the initial population region of genetic algorithm is selected from [0, 1]; its population size is 20; its crossover and mutation probabilities are 0.8 and 0.2, respectively; and its maximum iteration number is 100. Based on our model above, we can implement sequencing computations from LED ray radiation to the camera ray response; thus, the accurate output of wall lights can be calculated. After lighting control, the Eigenface method is used for face recognition. The Eigenface uses principal component analysis method to obtain the vector description of the face and considers the Euclidean distance to identify people. Its computational speed is very fast for our application.

$$\begin{aligned} &\arg\min\left\{M_F\right\} \\ &\text{s.t } I_{WLMIN} \le I_{WL\_i} \le I_{WLMAX} \quad (i = 1, 2, \ldots, 7) \\ &I_{OHL} \in \left(I_{OHL\_1}, I_{OHL\_2}, I_{OHL\_3}\right) \end{aligned} \tag{19}$$

where min{*} denotes computing the minimum of its variable; I_{WLMIN} and I_{WLMAX} are the minimum and maximum outputs of wall light intensities I_{WL_i} ($i = 1, 2, \ldots, 7$); and I_{OHL_1}, I_{OHL_2}, and I_{OHL_3} are the fixed outputs of overhead light intensity I_{OHL}.

IV. EXPERIMENTS AND DISCUSSIONS

A distributed lighting system was developed, several face images were accumulated, and a series of test experiments were conducted to confirm the effectiveness of the proposed method. The simulation programs were written by Python 3.6 and OpenCV 3.4.5 using our computer (2.4 GHz, 3 GB RAM).

A. Experiment System and Data

Fig. 10 shows images of our system, intensity distribution curves of lighting sources, and certain face image samples. In Fig. 10, (a) is the experimental system of wall lights; (b) shows the digital luminance meter and head support, which can be used to control the head pose; (c) is an industrial prototype system of (a), and its cosmetic designing looks similar to a

flower to fulfill the application requirement of entertainment places; (d) shows the binocular camera; (e) is the overhead light; (f) is the control circuit box; (g) and (h) are the intensity distribution curve examples of the overhead and wall lights; (i) to (m) are face image samples. Table 2 lists out the system installation parameters (see Fig. 3). Without loss of generality, the maximum intensity outputs of overhead and wall lights are set by 3 and 6 degrees in our experiment, respectively. Because there will be excess output methods in the overhead and wall light settings, only certain examples are shown. Tables 3 and 4 are the parameter setting methods of Figs. 10 (g) and (h); Table 5 presents the wall light control methods of Figs. 10 (i) - (m). As shown in Fig. 10, face shadows and details are influenced by the wall lights; thus it is necessary to control their outputs elaborately to improve face imaging effects.

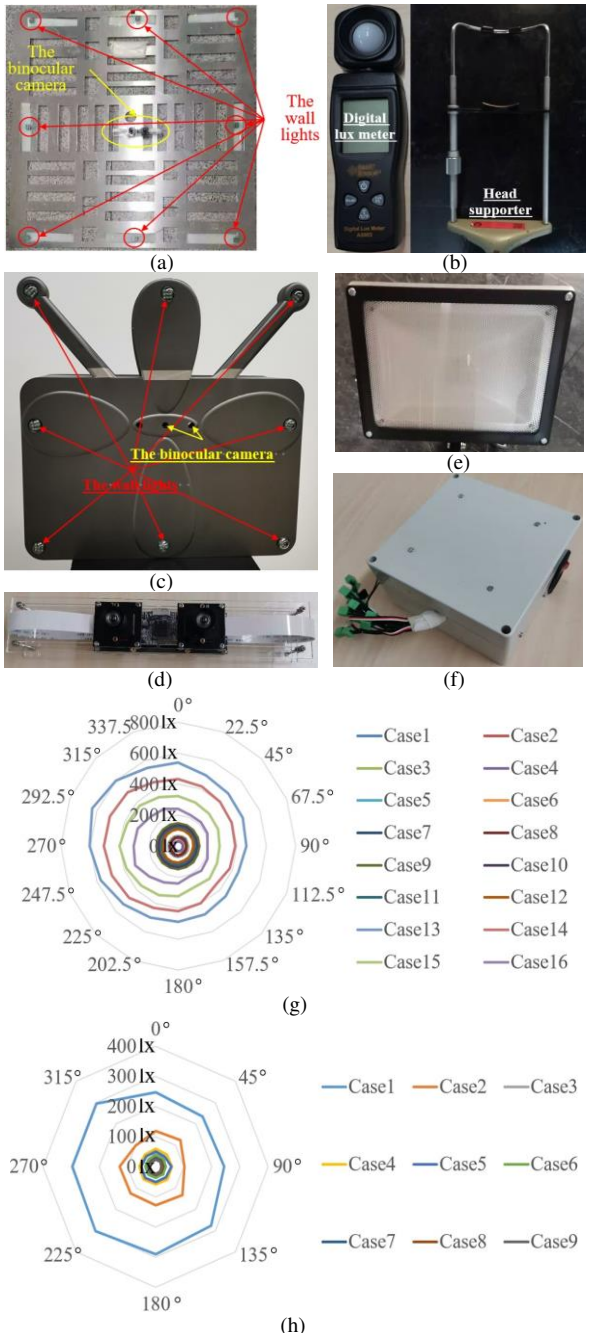

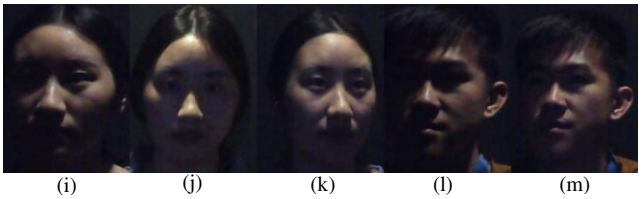

Fig. 10. Images of the experimental system, intensity distribution curves of lighting sources, and face image data samples (the intensity of the overhead light is degree 2, and the intensities of wall lights are shown in Table 5).

TABLE II
EXPERIMENTAL PARAMETERS SETTING METHODS OF FIG. 3

Distance (cm)					
D_0	D_1	D_2	D_3	D_4	D_5
280.0	15.0	50.0	85.0	150.0	45.0
D_6	D_7	D_8	D_9	D_{10}	D_{11}
45.0	12.0	45.0	45.0	5.5	15.0

TABLE III
EXPERIMENTAL PARAMETERS SETTINGS OF FIG. 10 (G)

Overhead light output intensity degree 2		Observation radius (cm)			
		9	16	25	36
Installation height (cm)	50.0	Case1	Case2	Case3	Case4
	100.0	Case5	Case6	Case7	Case8
	150.0	Case9	Case10	Case11	Case12
	200.0	Case13	Case14	Case15	Case16

TABLE IV
EXPERIMENTAL PARAMETERS SETTINGS OF FIG. 10 (H)

Installation height of wall light LED (30.0 cm)		Observation radius (cm)		
		4.5	8	12.5
Output intensity degree	1	Case1	Case2	Case3
	3	Case4	Case5	Case6
	6	Case7	Case8	Case9

TABLE V
INTENSITY SETTINGS OF WALL LIGHTS OF FIGS. 10 (I) TO (M)

Name	I_{WL_0}	I_{WL_1}	I_{WL_2}	I_{WL_3}	I_{WL_4}	I_{WL_5}	I_{WL_6}	I_{WL_7}
(i)	0	0	0	0	0	0	0	0
(j)	0	0	0	0	0	0	0	0
(k)	3	3	3	3	3	3	3	3
(l)	5	5	5	5	5	5	5	5
(m)	3	3	3	3	3	3	3	3

B. Results of Face Detection and Facial Landmark Extraction

Face detection and facial landmark extraction were performed; moreover, the camera calibration accuracy was evaluated. Figs. 11 (a) - (e) are the face detection and 2D facial landmark extraction results of Figs 10 (i) - (m); Figs. 11 (f) - (j) are the 3D computational results of 2D facial landmarks in the camera coordinate system; (k) shows the definitions of the head pose angles α, β, and γ; (l) shows photo samples of a calibration object in this experiment. Table 6 shows the results of the intrinsic and extrinsic parameters of the binocular camera (see equation (1)); Table 7 shows its accuracy evaluation results. Here, the average length error of the metal rod in (l) was ≤ 1.06% of its actual length. Further analyses demonstrated that the calibration accuracy of z-axis in the camera coordinate system was lower than the accuracy of x- or y-axis. In this study, performing error analysis of the entire vision system is a difficult task because the final recognition results are associated with multiple factors such as the extraction accuracy or 3D measurement accuracy. Because the final recognition results

have proved the effectiveness of our method, we believe that the binocular measurement errors above are tolerable.

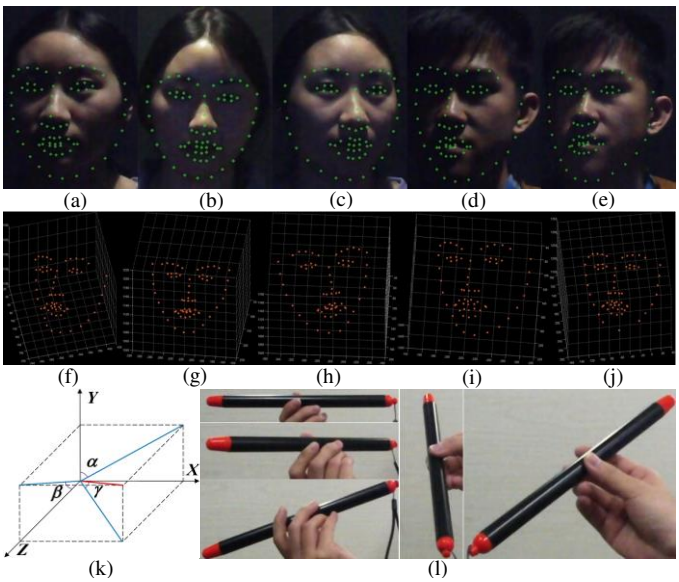

Fig. 11. Results of face detection, 2D/3D facial landmarks extractions, coordinate definitions of head pose angles, and calibration experiment data.

TABLE VI
INTRINSIC AND EXTRINSIC PARAMETERS OF BINOCULAR CAMERA

Left camera intrinsic parameters [a]	f_x	f_y	u_0	v_0
	886.216 ± 4.266	887.052 ± 4.204	640.874 ± 3.749	322.348 ± 3.675
Right camera intrinsic parameters	f_x	f_y	u_0	v_0
	885.431 ± 4.295	885.511 ± 4.227	635.795 ± 3.726	362.868 ± 3.594
Camera extrinsic parameters	r_{00}	r_{01}	r_{02}	r_{10}
	0.999997	-0.001775	-0.001935	-51.978
	r_{11}	r_{12}	r_{20}	r_{21}
	0.001765	0.999984	-0.005462	-0.337
	r_{22}	t_0	t_1	t_2
	0.001945	0.005458	0.999983	-1.077

[a] The pixel size is 3.75 μm × 3.75 μm; the units of f_x, f_y, u_0, and v_0 are pixels.

TABLE VII
MEASUREMENT RESULTS OF METAL ROD USING BINOCULAR CAMERA

Experiment results of angles (°)			Length measurement result / practical length (cm)
α	β	γ	
-89.52713	-89.85539	0.00128	237.06490±0.00455 / 240.0
-89.07383	-1.44892	42.18978	240.01840±0.01393 / 240.0
-66.72375	-80.36320	20.69985	240.19387±0.00439 / 240.0
-41.28552	-74.98541	25.03220	240.82481±0.011359 / 240.0
-51.75594	-43.06375	48.66396	242.64855±0.01823 / 240.0

C. Results of 3D Face and Coordinate Transformation Computations

The 3DMM was used to analyze the 3D structure of face. Unlike the face recognition in a bright field, face data captured in a dark field will be severely affected by shadow; therefore, an adaptive MSR is used: both shadow features and SVM are considered to tune the control parameter ε_3 of MSR (see (4)). From Fig. 6, after the 68 facial landmarks are extracted, the mean value features in six image blocks will be computed. Their center coordinates, widths, and heights are defined in Table 8. From Table 8, the image blocks can be regulated by selected facial landmarks; therefore, the estimation effects of face shadows are comparably stable. Figs. 12 (a) and (b) are the shadow sampling results of Figs. 10 (j) and (m). Table 9 shows the SVM evaluation results of the adaptive MSR. The training data are the means of six image blocks, and its supervising data are the subjective evaluations of the imaging effect. From Table 9, SVM with a Gaussian kernel function can achieve the best prediction accuracy, and its results can be ≥ 85.0%.

TABLE VIII
SAMPLING METHODS OF SIX IMAGE BLOCKS IN FIG. 6

Image block	Block center coordinate	Width	Height
1	(Abscissa of facial landmark 36, ordinate of facial landmark 40)	L_1[a]	L_2[b]
2	(Abscissa of facial landmark 42, ordinate of facial landmark 46)	L_1	L_2
3	(Difference between the abscissa of facial landmark 33 and L_1, ordinate of facial landmark 32)	$2\times L_1$	L_2
4	(Difference between the abscissa of facial landmark 57 and L_1, ordinate of facial landmark 58)	$2\times L_1$	L_2
5	(Abscissa of facial landmark 39, ordinate of facial landmark 28)	L_2	L_1
6	(Abscissa of facial landmark 42, ordinate of facial landmark 28)	L_2	L_1

[a] L_1 is the difference between abscissas of facial landmarks 39 and 36; [b] L_2 is the difference between ordinates of facial landmarks 40 and 37.

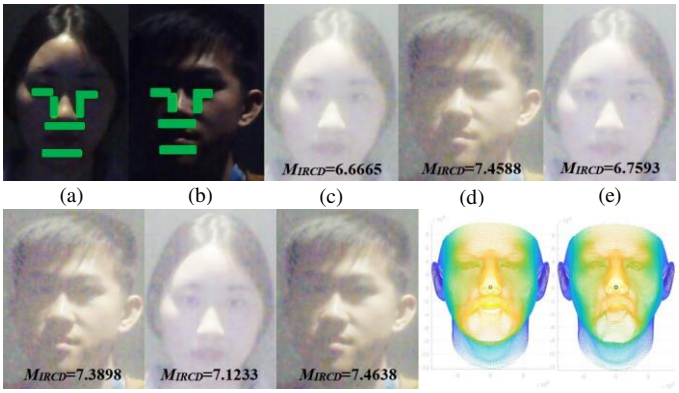

Fig. 12. Image enhancement effect evaluation results and 3DMM computational results.

TABLE IX
TRAINING PRECISION COMPARISONS OF SVM

Num	Training/test data amount	Kernel function	Prediction accuracy
1	390/98	Linear	46.9%
2	496/124	Linear	54.8%
3	496/124	Polynomial	61.2%
4	390/98	Polynomial	63.3%
5	496/124	Gaussian	**85.8%**
6	390/98	Gaussian	**87.5%**

Figs. 12 (c) - (h) show the MSR comparison results of Figs. 10 (j) - (m). An image quality evaluation metric M_{IRCD} (see (20)) is then used to assess the MSR. The larger the M_{IRCD}, the better the imaging contrast (detail). The 3DMM can obtain a better estimation result using images with additional detail. In Fig. 12, considering the first experiment, the MSR parameters of (c) and (d) are set by $\varepsilon_1 = 71$, $\varepsilon_2 = 225$, and $\varepsilon_3 = 31$; (d) can obtain a better processing effect. In the second experiment, the parameters of (e) and (f) are set by $\varepsilon_1 = 71$, $\varepsilon_2 = 225$, and $\varepsilon_3 = 3$; (f) obtains a better effect. Here, these abovementioned experiments use fixed empirical values to implement MSR

computations, thus their processing effects are unstable. In the third experiment, the parameters of (g) and (h) are $\varepsilon_1 = 71$, $\varepsilon_2 = 225$, and $\varepsilon_3 = 17$, as well as $\varepsilon_1 = 71$, $\varepsilon_2 = 225$, and $\varepsilon_3 = 5$; where ε_3 is computed by SVM. Our method can obtain the best effect as per M_{IRCD}. Figs. 12 (i) and (j) are the 3DMM results of (g) and (h), respectively. In this study, data processing is performed in the camera coordinate system; therefore, the coordinate transformation should be estimated by (2). The corresponding result samples are shown in Table 10.

$$M_{IRCD} = \frac{\eta}{k_1 k_2} \sqrt{\sum_{i=1}^{k_1}\sum_{j=1}^{k_2}\left[\frac{\lg\left|I_{i,j} - \sum_{c=1}^{3}\lambda_c\left(\left(I_{c1}+\ldots+I_{cn}\right)/n\right)\right|}{\lg\left|I_{i,j} + \sum_{c=1}^{3}\lambda_c\left(\left(I_{c1}+\ldots+I_{cn}\right)/n\right)\right|}\right]^{\rho}} \quad (20)$$

where $k_1 \times k_2$ is the image block quantity of entire image; $I_{i,j}$ is the grey value of center pixel; n is the pixel quantity of image block; $(I_{c1}+\ldots+I_{cn})/n$ is the average intensity of image block; λ_c is the weights of each color component, λ_c can be λ_r, λ_g, or λ_b, with $\lambda_r = 0.299$, $\lambda_g = 0.587$, and $\lambda_b = 0.144$; $\eta = 1000$; $\rho = 0.08$.

TABLE X
SAMPLES OF TRANSFORMATION MATRICES OF EQUATION (2)

Image name	R_{Cam_3DMM}	T_{Cam_3DMM}
Fig. 10 (j)	$\begin{bmatrix} 0.000989 & -0.000258 & 0.000194 \\ -0.000103 & -0.000845 & -0.000599 \\ 0.000306 & 0.000550 & -0.000829 \end{bmatrix}$	$\begin{bmatrix} -344.142999 \\ 145.796679 \\ 1241.533534 \end{bmatrix}$
Fig. 10 (m)	$\begin{bmatrix} 0.000934 & -0.000111 & 0.000091 \\ -0.000062 & -0.000853 & -0.000402 \\ 0.000130 & 0.000391 & -0.000850 \end{bmatrix}$	$\begin{bmatrix} -279.232146 \\ 132.244239 \\ 1159.143578 \end{bmatrix}$

D. Results of Face Lighting Effect Evaluation

To estimate the 3D face lighting effect, the sequencing computations of LED radiation intensity, ray reflection luminance, camera response, and face lighting uniformity were performed. Fig. 13 and Table 11 show the results. In Fig. 13, test images are the images (j) and (m) in Fig. 10; the computed LUOPs and the fitted simplified head models are shown in (a) and (b); and each facet normal vector of (a) and (b) is marked by a line with a circle at its end in (c) and (d). When calculating the LED lighting effect, each wall light is considered as a point source and the overhead light is regarded as a point source array. Then ray reflection luminance can be calculated using the sum of a point-to-point computation. When estimating the facet normal vector of LUOPs, since the 3DMM includes more than 50,000 points, some vertexes of triangular patch can be selected close to the LUOPs; then we can use any 3 vertexes to estimate the facet normal vector. Other unit vectors, such as $\boldsymbol{L_{ij}}$ or $\boldsymbol{V_i}$, can be assessed using two spatial points in the camera coordinate system. To illustrate sufficient details of 3DMM, the x, y, and z coordinate magnitudes are set to be extremely large in Fig. 13.

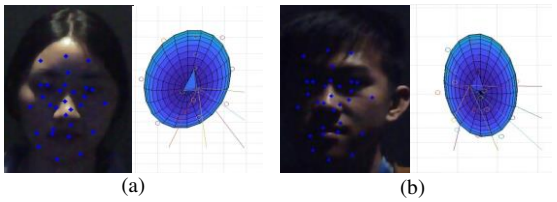

(a) (b)

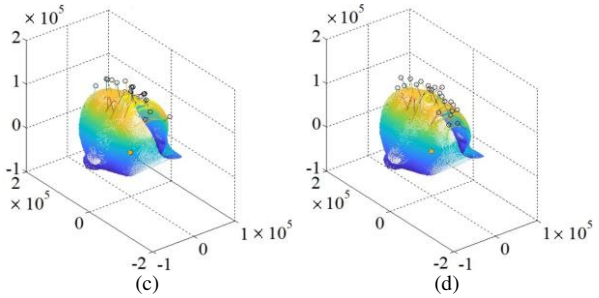

(c) (d)

Fig. 13. LUOPs, ray occlusion judgement results, and facet normal vectors of Figs. 10 (j) and (m).

TABLE XI
COMPUTATIONAL RESULTS OF REFLECTION LUMINANCE AND CAMERA RESPONSE OF FIGS. 13 (A) AND (B)

Results of reflection luminance and camera response of Fig. 13-(a), where $E_s = 27.55$				
Point 1	Point 2	Point 3	Point 4	Point 5
61.02/18.50	79.44/24.54	98.67/30.92	77.57/23.89	57.46/17.26
Point 6	Point 7	Point 8	Point 9	Point 10
60.15/18.18	87.93/27.23	96.61/30.07	76.58/23.49	73.69/22.48
Point 11	**Point 12**	Point 13	Point 14	Point 15
61.05/18.46	**20.57/6.27**	48.34/14.29	56.82/17.08	58.59/17.58
Point 16	Point 17	Point 18	Point 19	Point20
42.04/12.78	45.45/13.96	65.59/20.13	87.74/27.13	90.70/28.22
Point 21	Point 22	Point 23	Point 24	Point 25
23.04/6.77	54.45/16.67	69.70/21.13	27.02/7.91	54.55/16.14
Point 26	Point 27	Point 28	Point 29	Point 30
35.89/10.77	41.36/12.40	5.39/1.63	55.59/16.55	67.20/20.24
Results of reflection luminance and camera response of Fig. 13-(b), where $E_s = 5.73$				
Point 1	Point 2	Point 3	Point 4	Point 5
11.25/3.15	18.26/5.26	17.79/5.28	18.48/5.32	11.81/3.28
Point 6	Point 7	Point 8	Point 9	Point 10
11.42/3.20	24.26/7.11	27.21/8.04	12.63/3.63	11.67/3.33
Point 11	Point 12	Point 13	Point 14	Point 15
3.97/1.12	16.13/4.62	8.21/2.23	11.18/3.11	11.44/3.19
Point 16	Point 17	Point 18	Point 19	Point20
0.01/0.0	18.89/5.46	21.45/6.22	24.99/7.33	28.99/8.63
Point 21	Point 22	Point 23	Point 24	Point 25
5.01/1.36	22.82/6.63	16.83/4.80	9.18/2.49	13.10/3.62
Point 26	Point 27	Point 28	Point 29	Point 30
18.11/5.13	1.74/0.49	16.60/4.73	10.17/2.82	16.11/4.57

The processing effect of ray occlusion was also evaluated. Fig. 13 and Table 11 present the computational results of Figs. 10 (j) and (m). The fitted simplified head models are illustrated in Fig. 13 (a) and (b); the fitting results of one ellipsoid and three planes are also shown in Table 12. Clearly, some ray occlusion accidents can be found in the table. For example, points 12 and 16 are affected by the occlusion problem. Note that a small camera response does not mean that ray occlusion has occurred. In Table 11, the camera response intensity of observation point 28 is smaller than that of point 12; however, ray occlusion does not occur there. After a series of tests, we found that ray occlusion will be easily observed in the cheek or near the nose of subject when the absolute value of the head pose angle γ (see Fig. 11 (k)) is ≥ 15.0 º; otherwise, if the absolute value of γ is comparable small (e.g., $\gamma < 10.0$ º), ray occlusion will always occur close to the nose. Changing the head pose angles α and β may create some ray occlusions; however, considering our typical application, these cases are not investigated.

TABLE XII
RESULTS OF RAY OCCLUSION EVALUATION OF FIGS. 13 (A) AND (B) IN THE 3D CAMERA COORDINATE SYSTEM

Image name	Ellipsoid function	Plane functions	Ray occlusion incident
Fig. 13 (a)	The ellipsoid center coordinate is (-113.40, 101.87, 988.37), the ellipsoid radiuses are 39.35, 58.61, 17.53; and their corresponding direction vectors are (0.980, 0.155, -0.129), (0.155, -0.988, -0.007), and (0.129, 0.013, 0.992), respectively.	The plane functions are $223664 - 128 \times y - 234 \times z - 142 \times x = 0$, $31 \times y - 259 \times x + 30 \times z - 59503 = 0$, and $22 \times x + 116 \times y - 108 \times z + 95176 = 0$.	The occluded LUOP is the point 12, its coordinate is (-107, 80, 977), the occluded wall light coordinate is (-450, -450, 0).
Fig. 13 (b)	The ellipsoid center coordinate is (-270.57, 92.78, 1051.76); the ellipsoid radiuses are 45.87, 76.93, and 24.41; and their corresponding direction vectors are (0.996, 0.049, -0.081), (-0.027, 0.967, 0.253), and (0.091, -0.249, 0.964), respectively.	The plane functions are $234 \times x + 238 \times y + 190 \times z - 155698 = 0$, $364 \times x - 132 \times y - 56 \times z + 168420 = 0$, and $234 \times z - 78 \times y - 52 \times x - 255710 = 0$.	The occluded LUOP is the point 16, its coordinate is (-286, 76, 1082), the occluded wall light coordinate is (450, 0. 0)

After computing LUOPs, both DTW and variance features were used to assess the lighting effect. The DTW was employed to assess the lighting effect between the point set captured from the standard lighting environment and the set recorded from the arbitrary environment. Fig. 14 shows the standard and our intensity series of 30 LUOPs; some experimental image data are also shown in Fig. 15. When building the standard series, 24 images are used and their lighting effects are good (e.g., environment illuminance is ≥ 250.0 lx) for face recognition. In Fig. 14, the LUOPs of Figs. 10 (i) - (m) are illustrated in the form of time series data. From Fig. 14, the diversities among the standard and experimental series are remarkable. When computing a variance feature, its numerator represents lighting uniformity, whereas the inverse of its denominator shows the contrast between the face character (eyes, nose, or mouth) and the cheek. Table 13 shows certain computational results of LUOPs. From Table 13, M_F even can be used as a parameter to predict the face recognition result. For example, when M_F is ≤ 39.8, almost the entire face can be correctly recognized.

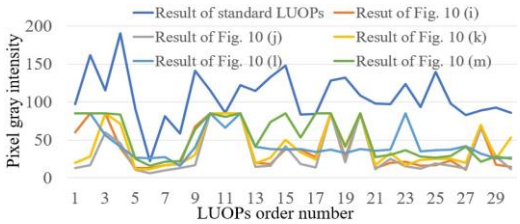

Fig. 14. LUOP intensity series of the standard image and our experimental images in Figs. 10 (i) - (m).

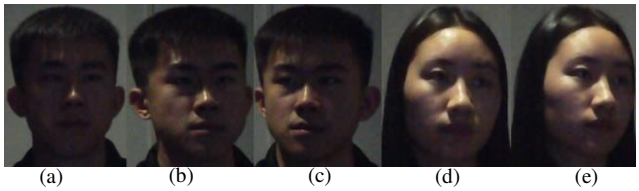

Fig. 15. Image data of face uniformity and recognition evaluation experiment.

TABLE XIII
FACE UNIFORMITY AND FACE RECOGNITION RESULTS

Image name	Face uniformity			
	M_{DTW}	M_{VAR}	M_F	Face recognition result
Fig. 10 (i)	29.3611	92.1327	121.4938	Fail
Fig. 10 (j)	25.8111	14.0052	39.8163	Fail
Fig. 10 (k)	22.2088	10.026	32.2348	Success
Fig. 10 (l)	29.4552	18.6753	48.1305	Fail
Fig. 10 (m)	29.0497	23.2506	52.3003	Fail
Fig. 15 (a)	16.5146	61.6042	78.1188	Fail
Fig. 15 (b)	10.3217	14.2543	24.5761	Success
Fig. 15 (c)	12.3227	26.9576	39.3803	Success
Fig. 15 (d)	14.1835	25.7998	39.9833	Success
Fig. 15 (e)	14.8588	20.8301	35.6889	Success

E. Results of Lighting Compensation and Face Recognition

An effect evaluation experiment of intelligent lighting compensation was performed. Fig. 16 shows the imaging results before and after compensation. In Fig. 16, (a) - (j) are the original images, and (k) - (t) are the compensation results. To control subjects' head poses and implement tests, image data captured before and after lighting control were not recorded in a one-time experiment. Table 14 presents the control methods of wall lights in Fig. 16. As shown in Fig. 16, the subjective imaging effect will be improved after lighting control. To confirm this conclusion, the face lighting uniformity index (see (17)) was investigated. Table 15 shows the computational results. From Table 15, the lighting uniformity index M_F can be decreased using our system, and face recognition accuracy can be improved. If sufficient image data are accumulated, M_F can be used to evaluate face recognition accuracy preliminarily and provide advice on lighting system installation.

Fig. 16. Imaging results before and after lighting compensation.

TABLE XIV
LUMINOUS INTENSITY CONTROL RESULTS OF WALL LIGHTS OF FIG. 16

Image name [a]	I_{WL_0}	I_{WL_1}	I_{WL_2}	I_{WL_3}	I_{WL_4}	I_{WL_5}	I_{WL_6}	I_{WL_7}
Fig. 16 (a)	3	3	3	3	3	3	3	3
Fig. 16 (b)	3	3	3	3	3	3	3	3
Fig. 16 (c)	3	3	3	3	3	3	3	3
Fig. 16 (d)	0	0	0	0	0	0	0	0
Fig. 16 (e)	0	0	0	0	0	0	0	0
Fig. 16 (f)	0	0	0	0	0	0	0	0
Fig. 16 (g)	3	3	3	3	3	3	3	3
Fig. 16 (h)	0	0	0	0	0	0	0	0
Fig. 16 (i)	3	3	3	3	3	3	3	3
Fig. 16 (j)	3	3	3	3	3	3	3	3
Fig. 16 (k)	3	6	5	6	5	5	6	4
Fig. 16 (l)	1	4	2	3	4	5	4	4
Fig. 16 (m)	4	6	3	5	5	5	6	3
Fig. 16 (n)	1	4	4	4	1	2	5	5
Fig. 16 (o)	6	6	6	6	6	6	6	6
Fig. 16 (p)	4	4	1	1	2	5	1	2
Fig. 16 (q)	4	3	1	5	3	5	1	2
Fig. 16 (r)	6	2	6	5	1	3	4	6
Fig. 16 (s)	2	6	5	3	5	3	3	5
Fig. 16 (t)	4	5	3	4	1	5	5	4

[a] The output intensity of overhead light is degree 2 (see Fig. 10 (g) and Table 3).

TABLE XV
FACE UNIFORMITIES AND FACE RECOGNITION RESULTS OF FIG. 16

Image name	M_F	Face recognition result	Image name	M_F	Face recognition result
Fig. 16 (a)	61.4983	Fail	Fig. 16 (k)	35.0119	Success
Fig. 16 (b)	137.5457	Fail	Fig. 16 (l)	31.1742	Success
Fig. 16 (c)	61.4079	Fail	Fig. 16 (m)	24.7103	Success
Fig. 16 (d)	37.6893	Fail	Fig. 16 (n)	26.9650	Success
Fig. 16 (e)	48.1652	Fail	Fig. 16 (o)	36.3809	Success
Fig. 16 (f)	55.1528	Fail	Fig. 16 (p)	29.6738	Success
Fig. 16 (g)	78.4229	Fail	Fig. 16 (q)	24.8963	Success
Fig. 16 (h)	70.7062	Fail	Fig. 16 (r)	26.7885	Success
Fig. 16 (i)	93.6827	Fail	Fig. 16 (s)	23.6204	Success
Fig. 16 (j)	79.7259	Fail	Fig. 16 (t)	21.0469	Success

A face recognition evaluation experiment was conducted using images captured by the near-infrared camera, the traditional visible light camera, and our proposed system. Different face recognition methods, such as Eigenface method, the traditional neural network-based method, and deep learning-based techniques, were tested. Table 16 lists the experimental results. The training data points were 520, and the test data points were 150 for each experiment. The subjects' heights ranged from 1.60 to 1.80 m; they were not required to face the central camera exactly during the experiments. Other experimental parameters in Table 3 were also used. The near-infrared camera in Kinect 1.0 and an ordinary visible light camera in our system (see Fig. 10 (d)) were used to capture image data. The output intensity of the overhead light was set by degree 2. The main response spectrum range of the near-infrared camera was ~ 950 nm. The intelligent wall light control method was used to construct the datasets.

Table 16 shows the evaluation results of both the algorithm processing speed and face recognition accuracy. The table shows that our system achieves the best performance. Regarding the recognition accuracy challenges, the Eigenface method can achieve the best result because of its simpleness and small training data requirement. The inability of the traditional neural network and sparse representation-based methods to obtain the best performance may be attributed to the small amount of training data and the improper feature description. Similarly, the inability of the deep learning-based method to obtain the best result may be attributed to the small amount of training data. A variant of the BoostGAN-based method [39] was considered in this experiment; however, because of the limited amount of training data, it was not simulated in this study. As for the processing speed, the computation of the intelligent lighting method will cost 1.07 s, and we believe it is sufficiently fast for our current application. The above results can confirm the effectiveness of our system and method to some extent.

TABLE XVI
FACE RECOGNITION ACCURACY COMPARISONS AND TIME CONSUMPTION EVALUATIONS USING DIFFERENT PHOTOGRAPHY METHODS AND FACE RECOGNITION ALGORITHMS

	Near-infrared camera		Traditional visible light camera				Our system				
			Time consumption (s)				Time consumption (s)				
	Recognition time (s)	RA [a]	MSR [b]	Face detection	Face recognition	RA	MSR	Face detection	Lighting control	Face recognition	RA
Eigenface method	0.909×10^{-4}	88.89%	0.617	0.143	0.211×10^{-3}	87.50%	0.617	0.143	1.07	0.150×10^{-3}	**99.61%**
Neural network-based method [32]	0.20×10^{-2}	85.71%	0.617	0.143	0.220×10^{-2}	92.76%	0.617	0.143	1.07	0.86×10^{-2}	94.01%
Sparse representation-based method [33]	0.109×10^{-1}	77.78%	0.617	0.143	0.213×10^{-1}	95.87%	0.617	0.143	1.07	0.187×10^{-1}	99.30%
AlexNet-based method [34]	0.867×10^{-2}	90.91%	0.617	0.143	0.484×10^{-2}	96.30%	0.617	0.143	1.07	0.483×10^{-2}	98.55%
FaceNet method [35]	0.732	55.56%	0.617	0.143	0.703	<50.0%	0.617	0.143	1.07	0.723	52.54%
DeepID method [36]	0.296	95.7%	0.617	0.143	0.288	93.75%	0.617	0.143	1.07	0.281	95.87%
DeepFace method [37]	0.176	89.53%	0.617	0.143	0.184	86.47%	0.617	0.143	1.07	0.163	87.15%
Deep cascade model method [38]	0.776×10^{-2}	96.12%	0.617	0.143	0.234×10^{-1}	97.45%	0.617	0.143	1.07	0.210×10^{-1}	97.45%

[a] RA means the face recognition accuracy; [b] MSR is our proposed MSR enhancement method (see Section 3.3) in this Table.

F. Discussions

In contrast to the face recognition in a bright field, the application in the dark field has additional difficulties. First, missing details caused by low contrast makes face recognition difficult. Currently, feature extraction cannot be separated from image processing at the pixel level. Therefore, the poor imaging detail and contrast in the dark field will decrease the recognition effect. Second, strong imaging noise always degrades recognition accuracy. The noise exists in the imaging system extensively, such as fixed pattern noise or random noises [40]. When environment luminance is high, the signal response of the imaging sensor is strong, and the noise is submerged by imaging signal; on the contrary, the noise can be detected clearly. Third, the negative influences of shadows and glare are another issue. They can be easily observed in the forehead, eyes, nose, and mouth. When the light source direction is improper, face features may be covered by the shadow or glare in some scenarios. All these factors will add difficulties to the face recognition.

Integrated lighting effect analysis of the wall lights was performed by DIALux 8.0. Fig. 17 shows the top view sketch map of the experiment, simulations of the illuminance distribution of the wall lights, and the relationship curve between the observation distance D_{13} and the illuminance intensity of the wall lights. In Fig. 17, (a) is the top view sketch map of the experiment, and points A and B mark the observation positions of a subject; (b) is the simulation results of DIALux, the 3D model of wall lights, an example of the front view illuminance distribution of the wall lights (D_{13} = 90.0 cm), and a color bar are shown; and (c) is the relationship curves between the observation distance and the illuminance intensity of points A and B (D_{12} = 45.0 cm). The distance of D_{12} is set by considering the approximate shoulder width of people and his or her standing pose. As shown in Fig. 17, if the observation distance is ≤ 150.0 cm, then the illuminance of the wall lights can be ≥ 15.0 lx. The practical experiment indicated if the surface lighting intensity of the face was ≥ 15.0 lx, the face recognition effect would be acceptable.

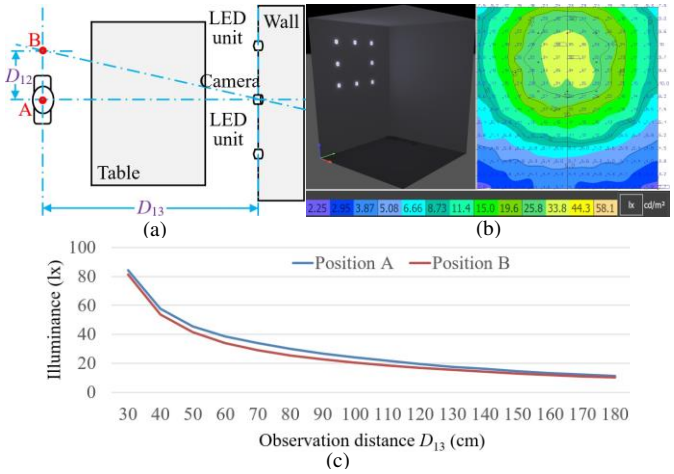

Fig. 17. Top view sketch map of analysis experiment, simulation results of the illuminance distribution of wall lights, and relationship curve between the observation distance and the illuminance intensity.

Both the wall and overhead lights were used in our system. Its main design concept is to use multi-light sources to provide a wide-range lighting compensation for the face. Considering the spatial layout constraint, the appearance design requirement, and even the government management regulation, a rectangle shape design mode was considered in this study. A standard commercial overhead light was used whose output power ranges from 10.0 to 20.0 W. A series of low-power wall lights (1.0 W) were also utilized. Fig. 18 shows the relationship among the luminance of overhead light, the luminance degree of the wall lights array (see Fig. 10 (h) and Table 5), and the lighting uniformity index M_F. From Fig. 18, if the luminance of the overhead light is ≥ 100.0 lx or 110.0 lx (the measurement position lies in the vertex of a subject's head), or the integrated luminance intensity of the wall lights is ≥ 10.0 lx (the measurement position locates in the subject's nose), the occurrence probability of low M_F (e.g., it is less than a threshold 40.0) will be high. Clearly, a large M_F index indicates a poor face recognition result (see Table 13).

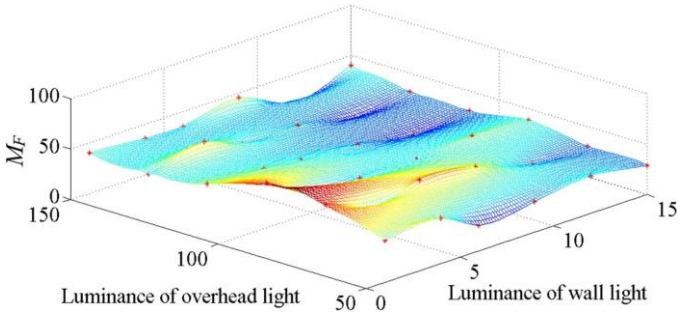

Fig. 18. Relationship among the luminance of overhead light, luminance of wall light array, and lighting uniformity index M_F.

A distributed design of lighting source was used in this study. High recognition accuracy cannot be achieved if the overhead light and the wall lights are separately used; and it can be found that the intelligent control of LED is better than the non-intelligent control method. Table 17 compares the results of an independent overhead light, an independent wall lights, an overhead light with fixed wall lights compensation (the output intensity degree is 3), and an overhead light with intelligent wall light compensation. Table 17 shows that our method can achieve the best recognition result apparently. Another consideration is that the overhead light should be installed in the proper location. If the vertical height between the head vertex of a subject and the roof is D_{14} and the distance between the head vertex and the geometry center of the overhead light is D_{15}, our experiment results show that the face recognition accuracy is decreased if the angle $\theta = \arccos(D_{14} / D_{15})$ is ≤ 10.0 º. Clearly the face shadow may be created easily in these situations.

TABLE XVII
FACE RECOGNITION ACCURACY COMPARISONS USING DIFFERENT LIGHTING METHODS

Method name	The overhead light	The wall lights	The overhead light + the fixed wall lights	The overhead light + the intelligent wall lights
Recognition accuracy	87.01%	57.58%	88.31%	99.61%

The glare region with significant number pixels should be avoided because the LUOPs may be submerged by it. The glare is mainly caused by the improperly setting the overhead light. The wall lights cannot produce glare because of their low power output. For example, if the output intensity of the overhead light is ≥ 150.0 lx in the head vertex, glare analysis should be considered. If the number of pixels of the glare region is ≥ 2500, the intensity of the overhead light should be decreased. In this study, glare detection can be performed after the MSR enhancement. The threshold-based segmentation can be used. After a series of tests, the glare always appears in the forehead, the nose, and even on the edge of cheek. Fig. 19 shows the processing effect of glare segmentation. In this experiment, the threshold was set to 200. In Fig. 19, (a) - (e) are the original images; (f) - (j) are the corresponding glare processing results. From Fig. 19, the fixed thresholding-based method can achieve a good glare segmentation performance for our application.

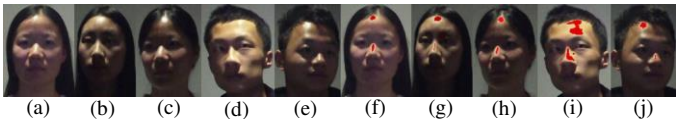

(a) (b) (c) (d) (e) (f) (g) (h) (i) (j)

Fig. 19. Experimental results of glare detection and segmentation.

The relationship between face lighting uniformity and recognition accuracy was investigated. Fig. 20 shows the results. Here the output of the overhead lighting was set by degree 2, and intelligent control of the wall lights was performed. Since it was difficult to accumulate sufficient images with the same M_F, lighting uniformity was segmented into several dispersed regions by K-means clustering first, e.g., they were [0, 20.0], [25.0, 33.0], [36.0, 47.0], [55.0, 63.0], and [75.0, 90.0], respectively. Then, we computed the recognition accuracy in each region and drew Fig. 20. The average number of training data points of Eigenface in each region was 70, and the average number of test data points was 20. From Fig. 20, the recognition accuracy is 100% when M_F is ≤ 33.0; and accuracy will remarkably decrease when the M_F belongs to [33.0, 63.0]. A gradual decrease in accuracy occurs when M_F is ≥ 63.0. Thus, if we can restrict M_F to [0.0, 33.0] by properly tuning the wall lights, high recognition accuracy may be achieved.

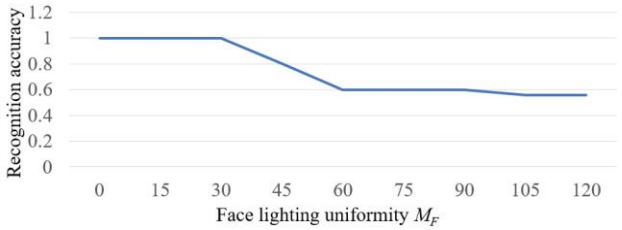

Fig. 20. Relationship between M_F and recognition accuracy.

The relationship between the head pose angle γ (Fig. 11 (k)) and face recognition accuracy was evaluated. The effects of other angles were not considered in this study for simplicity. Fig. 21 presents the results. In this experiment, both the overhead and wall lights were used, and the subjects were not asked to stand exactly in the axis position of the center camera. The output intensity of the overhead light was set by degree 2, and the outputs of the wall lights were controlled intelligently. The number of training data points in each sample angle was 513, and the corresponding number of test data points was 126. From Fig. 21, the best recognition accuracy is achieved when the pose angle γ is 0 º, i.e., when the subjects face up to the wall light panel. The lowest accuracy is obtained when the pose angle is -20 º. A shadow may be created, even with lighting compensation of the wall lights in such a situation. The fact that the recognition accuracy at 10 º is lower than that at 20 º may be attributed to the subjects' arbitrary standing positions.

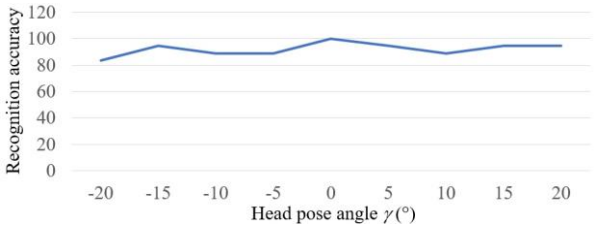

Fig. 21. Relationship between angle γ and recognition accuracy.

An experiment was conducted to assess lighting interference of the wall lights on a subject's eyes. First, the subject was asked to face the wall lights, with the head pose angle γ being 15 º and the standing distance D_{13} (see Fig. 17 (a)) being 150 cm. Second, some wall lights are lightened from the lowest to the highest levels continuously. If the subject detects dazzle during lighting control, he or she will report it. Third, these steps will be repeated under different output intensities of the overhead light and working modes of the wall lights. Table 18 shows certain results. The lightened wall lights IDs (see Fig. 3 (b)) are provided in the first row; the output intensities of wall lights when the dazzle can be noticed are shown in other rows. The greater the output intensity of overhead light, the higher the detected dazzle intensity of wall lights. The more lightened wall lights, the lower the detected dazzle intensity. In practice, a visitor will converse with the waitress, and his or her attention will be drawn to the waitress; thus, the detected dazzle intensity of wall lights may be greater.

TABLE XVIII
DAZZLE DETECTION EXPERIMENT RESULTS OF WALL LIGHTS

Detected dazzle intensity of wall lights		Output intensity of the overhead light (lx)		
		50	100	150
The lightened wall light IDs	1, 2, 3, 4, 5, 6, 7, 8	3	4	4
	1, 3, 6, 8	4	5	6
	1, 4, 6	5	5	6
	2, 7	none	none	none
	3, 5, 8	none	none	none
	1, 2, 3	none	none	none
	4, 5	4	4	5
	6, 7, 8	3	6	none

The computation effect of lighting uniformity evaluation index M_F (see (17)) will influence the recognition result. Three experiments were performed to compare different computation methods of M_F. In the first experiment, only the M_{DTW} was used to assess M_F. In the second experiment, only the M_{VAR} was considered. And in the third experiment, our M_F in (17) was used. After a series of tests, our method could achieve lighting control within 1.07 s and get the recognition accuracy by 99.61%. Other methods could realize lighting control in about 0.8 - 1.0 s, however their recognition accuracies were lower than 98.0%. From these results, although the lighting control time of our method was largest, its recognition accuracy was best. Moreover, its processing time was acceptable for our application. Therefore this method was used in our system finally. Other experiment results also showed less LUOPs would lead to poor recognition accuracy; and if we selected more LUOPs from face, the computation speed would drop.

Lots of models and their parameters are used in our system. Among these parameters, some can be directly computed by the measurement data, some have the definite physical meanings, and others can be proofed to be the best solutions for our application after experimental evaluations. For example, regarding the camera calibration, 2D and 3D coordinate transformation, 3DMM building, and 3DMM and camera coordinate transformation, no parameters need to be set because either the public 3DMM has been trained well or the corresponding parameters can be computed directly. As for the

shadow analysis, LED ray radiation, camera response estimation, and lighting uniformity evaluation, the parameters, which come from the MSR, SVM, LED model, and genetic algorithm, etc., will affect the recognition result definitely. However, because these parameters are derived from physical models, or some evaluation experiments have proofed their good performances, their values in Sections 3 and 4 are used.

Although the intelligent lighting concept has been invented for years, how to develop a lighting system with intelligence is still a problem. Some researches used environment perception sensors to tune the output of semiconductor lighting devices. Others considered hardware design [41] to implement lighting switching, energy saving, and online scheduling. Comparatively, environment perception-based lighting tuning is difficult to realize because rays are ubiquitous. How to process sensor data while considering accuracy and complexity is difficult. Fortunately, rapid advancements in imaging sensors, Internet Of Things (IOT) technique, and intelligent hardware offer this area a new development vitality. Imaging sensors can accurately perceive a 3D light field, IOT technique can flexibly construct a distributed system, and intelligent hardware can realize fast computation.

The proposed system has certain merits. First, its application effect is excellent. According to the experimental results, face recognition accuracy can be improved by at least 10.0%, particularly when the environment lighting is poor and complex. Second, its information processing ability is high, and many new artificial intelligence algorithms can be used in this system; e.g., new machine learning technique [42] can be developed to speed up the optimal lighting compensation. Third, the development cost of proposed system is low. Compared with certain infrared or near-infrared sensors, the LED light source and the mini-type visible light camera are inexpensive. Lastly, the application of the proposed system is flexible. Although a prototype system is defined in Fig. 3, the layout of LED units, however, has no limitation. If the spatial position between the LED units and the binocular camera is known, our proposed computational flow chart in Section 3.1 can be used.

Our system has certain limitations. Because the output power of the LED wall lights is small, it is only suitable for near scene applications currently. If far scene applications are required, the output power of the lighting system has to be increased which may cause a vision interference problem. The invisible lighting source may be considered in the future. Another problem is that the system processing speed is comparably slow, e.g., the optimal computation costs are ~ 1.8 seconds. This problem can be solved using a high performance hardware circuit. The vision disturbance problem (Table 18) should be avoided. Unlike the overhead light, which is fixed over people's head, the wall lights are installed to face people. A proper lighting field homogenization lampshade of LED units can then be developed. In the future, additional spatial layouts of LED units can be designed, and other machine learning methods can be used to improve the processing effect of our system.

V. Conclusion

A face lighting compensation system for dark-field applications is proposed. Unlike traditional methods, which attempt to use different sensors or improve existing recognition algorithms, our system uses distributed lighting compensation to enhance face recognition accuracy. One LED overhead light, eight LED wall lights, and a binocular camera are used to develop this system. The 3DMM with shadow analysis is used to build 3D faces. A shadow feature analysis-based adaptive MSR is used for 3DMM computation. After the sequencing computations of LED radiation, ray reflection, camera response, and lighting uniformity, intelligent system control can be solved by a genetic algorithm. Finally, the Eigenface method is used to perform face recognition. Experimental results have shown the performance of our system is robust and stable. In the future, different LED layout methods and face detection or recognition techniques with better processing performance will be studied to improve the usability of proposed system.

References

[1] S. Ouyang, T. Hospedales, Y.-Z. Song, X. Li, C. C. Loy, and X. Wang, "A survey on heterogeneous face recognition: sketch, infrared, 3D and low-resolution," *Image Vision Comput.*, vol. 56, pp. 28-48, Sept. 2016.

[2] Y. Li, S. Shan, M. Cui, C. Chu, and P. Hao, "Criminal victimization feature study of juveniles - the statistic results of S province," *China Youth Study*, vol. 4, pp. 61-66, Apr. 2014.

[3] C.-T. Huang, Z. Wang, and C.C. J. Kuo, "Visible-light and near-infrared face recognition at a distance," *J. Vis. Commun. Image R.*, vol. 41, pp. 140-153, Sept. 2016.

[4] N. Narang, and T. Bourlai, "Face recognition in the SWIR band when using single sensor multi-wavelength imaging systems," *Image Vision Comput.*, vol. 33, pp. 26-43, Nov. 2015.

[5] F. Nicolo, and N. A. Schmid, "Long range cross-spectral face recognition matching SWIR against visible light images," *IEEE T. Inf. Foren. Sec.*, vol. 7, no. 6, pp. 1717-1726, Dec. 2012.

[6] H. Sellahewa, and S. A. Jassim, "Image-quality-based adaptive face recognition," *IEEE T. Instrum. Meas.*, vol. 59, no. 4, pp. 805-813, Apr. 2010.

[7] M. Kopaczka, R. Kolk, J. Schock, F. Burkhard, and D. Merhof, "A thermal infrared face database with facial landmarks and emotion labels," *IEEE T. Instrum. Meas.*, vol. 68, no. 5, pp. 1389-1401, May 2019.

[8] H.-W. Lee, F.Pen, X.-Y. Lee, H. Dai, and Y. Zhu, "Research on face detection under different lighting," in *Proc. IEEE-ICASI*, Chiba, Japan, 2018, pp. 1145-1148.

[9] W. Mao, J. Chen, Y. Chen, S. S. Afshari, and X. Liang, "Construction of health indicators for rotating machinery using deep transfer learning with multiscale feature representation," *IEEE T. Instrum. Meas.*, vol. 70, pp. 3511313-1 – 3511313-13, Feb. 2021.

[10] B. Peng, W. Wang, J. Dong, and T. Tan, "Optimized 3D lighting environment estimation for image forgery detection," *IEEE. T. Inf. Foren. Sec.*, vol. 12, no. 2, pp. 479-494, 2017.

[11] C. Kauba, B. Proggegger, and A. Uhl, "Focusing the beam - a new laser illumination based data set providing insights to finger - vein recognition," in *Proc. IEEE-BTAS*, Redondo Beach, CA, USA, 2018, pp. 1-9.

[12] M. Myint, K., Yonemori, A. Yanou, K. N. Lwin, M. Minami, and S. Ishiyama, "Visual-based deep sea docking simulation of underwater vehicle using dual-eyes cameras with lighting adaptation," in *Proc. IEEE-OCEANS*, Shanghai, China, 2016, pp. 1-8.

[13] M. Zhou, H. Lin, J. Yu, S. Young, "Hybrid sensing face detection and recognition," in *Proc. IEEE-AIPR*, Washington, DC, USA, 2015, pp. 1-9.

[14] S. Y. Chun, and C.-S. Lee, "Applications of human motion tracking: smart lighting control," in *Proc. IEEE-CVPRW*, Portland, OR, USA, 2013, pp. 387-392.

[15] P. P. Srinivasan, B. Mildenhall, M. Tancik, J. T. Barron, R. Tucker, N. Snavely, "Lighthouse: predicting lighting volumes for spatially-coherent illumination," in *Proc. IEEE-CVPR*, Seattly, WA, USA, 2020, pp. 8077-8086.

[16] J. Yang, F. Zhang, B. Chen, and S. U. Khan, "Facial expression recognition based on facial action unit," in *Proc. IEEE-IGSC*, Alexandria, VA, USA, 2019, pp. 1-6.
[17] H. Nomani, and S. Sondur, "3D face generation from sketch using ASM and 3DMM," in *Proc. IEEE-ICACCT*, Sangamner, India, 2018, pp. 426-430.
[18] Z. Zhu, X. Jin, H. Yang, and L. Zhong, "Design of diffuse reflection freeform surface for uniform illumination," *J. Disp. Technol.*, vol. 10, no. 1, pp. 7-12, Jan. 2014.
[19] A. Malti, and A. Bartoli, "Combining conformal deformation and Cook-Torrance shading for 3-D reconstruction in laparoscopy," *IEEE T. Bio.-Med. Eng.*, vol. 61, no. 6, pp. 1684-1692, Jan. 2014.
[20] B. K. P. Horn, *Robot Vision*, MIT Press, Cambridge, MA, 1986.
[21] H. Liu, Q. Zhou, J. Yang, T. Jiang, Z. Liu, and J. Li, "Intelligent luminance control of lighting systems based on imaging sensor feedback," *Sensors*, vol. 17, no. 321, pp. 17020321-1 – 17020321-24, Feb. 2017.
[22] S. Y. Chen, J. Zhang, H. Zhang, N. M. Kwok, and Y. F. Li, "Intelligent lighting control for vision-based robotic manipulation," *IEEE T. Ind. Electron.*, vol. 59, no. 8, pp. 3254-3263, Aug. 2012.
[23] M. S. Hossain, and G. Muhammad, "Emotion-aware connected healthcare big data towards 5G," *IEEE Internet Things*, vol.5, no. 4, pp. 2399-2406, Aug. 2018.
[24] W. Zhang, Y. Bian, and F. Dong, "Comparation of calibration methods for bubbly flow video image," in *Proc. IEEE-CCDC*, Taiyuan, China, 2012, pp. 2602-2606.
[25] P. Koppen, Z. Feng, J. Kittler, M. Awais, W. Christmas, X. Wu, and H. Yin, "Gaussian mixture 3D morphable face model," *Pattern Recogn.*, vol. 74, pp. 617-628, Feb. 2018.
[26] H. Liu, H. Lu, and Y. Zhang, "Image enhancement for outdoor long-range surveillance using IQ-learning multiscale Retinex," *IET Image Process.*, vol. 11, no. 9, pp. 786-795, Sept. 2017.
[27] http://vision.ucsd.edu/~iskwak/ExtYaleDatabase/ExtYaleB.html
[28] M.-T. Lee, and M.-R. Tseng, "Efficient, long-life and Lambertian source of top-emitting white OLEDs using low-reflectivity molybdenum anode and co-doping technology," *Curr. Appl. Phys.*, vol. 8, pp. 616-619, Aug. 2008.
[29] M. Bitterlin, G. Bern, H. R. Wilson, A. Heimsath, and P. Nitz, "Physicla models of the bidirectional reflectance of solar receiver coatings," *Solar Energy*, vol. 209, pp. 653-661, Oct. 2020.
[30] B. Kar, A. Mukherjee, and P. K. Dutta, "Stroke point warping-based reference selection and verification of online signature," *IEEE T. Instrum. Meas.*, vol. 67, no. 1, pp. 2- 11, Jan. 2018.
[31] F. Capelli, J.-R. Riba, E. Ruperez, and J. Sanllehi, "A genetic-algorithm optimized fractal model to predict the constriction resistance from surface roughness measurements," *IEEE T. Instrum. Meas.*, vol. 66, no. 9, pp. 2437-2447, Sept. 2017.
[32] Z. Yu, F. Liu, R. Liao, Y. Wang, H. Feng, and X. Zhu, "Improvement of face recognition algorithm based on neural network," in *Proc. IEEE-ICMTMA*, Changsha, China, 2018, pp. 229-234.
[33] J. Wright, A. Y. Yang, A. Ganesh, S. S. Sastry, and Y. Ma, "Robust face recognition via sparse representation," *IEEE T. Pattern Anal.*, vol. 31, no. 2, pp. 210-227, Feb. 2009.
[34] W. Zeng, Q. Meng, and R. Li, "Design of intelligent classroom attendance system based on face recognition," in *Proc. IEEE-ITNEC*, Chengdu, China, 2019, pp. 611-615.
[35] F. Schroff, D. Kalenichenko, and J. Philbin, "FaceNet: a unified embedding for face recognition and clustering," in *Proc. IEEE-CVPR*, Boston, MA, USA, 2015, pp. 815-823.
[36] S. Y. Wong, K. S. Yap, Q. Zhai, and X. Li, "Realization of hybrid locally connected extreme learning machine with DeepID for face verification," *IEEE Access*, vol. 7, pp. 70447-70460, May 2019.
[37] S. Srisuk, and S. Ongkittikul, "Robust face recognition based on weighted DeepFace," In *Proc. IEEE-iEECON*, Pattaya, Thailand, 2017, pp. 1-4.
[38] L. Zhang, J. Liu, B. Zhang, D. Zhang, and C. Zhu, "Deep cascade model-based face recognition: when deep-layered learning meets small data," *IEEE T. Image Process.*, vol. 29, pp. 1016-1029, Sept. 2020.
[39] Q. Duan, and L. Zhang, "Look more into occlusion: realistic face frontalization and recognition with BoostGAN," *IEEE T. Neur. Net. Lear.*, vol. 32, no. 1, pp., 214-228, Mar. 2021.
[40] H. Liu, S. Yang, C. Guo, J. Li, M. Yan, and J. Lan, "Calibration of imaging sensor and fiber optic taper-caused distortion in an X-ray intensified CMOS camera," *IEEE Access*, vol. 7, pp. 185393-185407, Dec. 2019.
[41] S. Tang, V. Kalavally, K. Y. Ng, and J. Parkkinen, "Development of a prototype smart home intelligent lighting control architecture using sensors onboard a mobile computing system," *Energy Buildings*, vol. 138, pp. 368-376, Jan. 2017.
[42] Y. Guo, J. Zhang, J. Cai, B. Jiang, and J. Zheng, "CNN-based real-time dense face reconstruction with inverse-rendered photo-realistic face images," *IEEE T. Pattern Anal.*, vol. 41, no. 6, pp. 1294-1307, Jun. 2019.

Haoting Liu received PhD degree from Chinese Academy of Sciences in 2010. Now he is with the School of Automation and Electrical Engineering, University of Science and Technology Beijing as a professor. His research fields including image processing and pattern recognition, etc.

Na Zheng received her bachelor's degree from University of Science and Technology Beijing in 2019. Now she is pursue her master's degree in School of Automation and Electrical Engineering, University of Science and Technology Beijing.

Yuan Wang received her bachelor's degree from University of Science and Technology Beijing in 2019. Now she is pursue her master's degree in School of Automation and Electrical Engineering, University of Science and Technology Beijing.

Jiacheng Li received his Master's degree from University of Science and Technology Beijing in 2020. Now he is with the Intelligent Mine Research Institute, China Coal Research Institute.

Zhiqiang Zhang received the Ph.D. degree from University of Chinese Academy of Sciences, China, in 2010. Currently, he is a University Academic Fellow with University of Leeds. His research fields include wearable sensors and applications.

Yajie Li received her bachelor's degree from University of Science and Technology Beijing in 2020. Now she is pursue her master's degree in School of Automation and Electrical Engineering, University of Science and Technology Beijing.

Jinhui Lan received the Ph.D. degree from Beijing Institute of Technology in 1998. Now she is a professor with University of Science and Technology Beijing, China. Her research fields include image processing and intelligent instrument, etc.